Relativistic *R*-matrix studies of photoionization processes of Ar^{5+}*

Li Chuan-Ying(李传莹)[a)b)], Han Xiao-Ying(韩小英)[b)], Wang Jian-Guo(王建国)[b)], and Qu Yi-Zhi(屈一至)[a)†]

[a)] *College of Material Sciences and Optoelectronic Technology, University of Chinese Academy of Sciences, Beijing* 100049, *China*
[b)] *Institute of Applied Physics and Computational Mathematics, Beijing* 100088, *China*

(Received 26 March 2013; revised manuscript received 25 April 2013)

The 3s–*n*p photoionization processes of the ground state $^2P_{1/2}$ and the metastable state $^2P_{3/2}$ of Ar^{5+} are investigated using our recently developed relativistic *R*-matrix code, where the interactions between the bound states and the continuum states are included. Both resonance positions and the oscillator strengths are in much better agreement with the absolute experimental measurements by Wang *et al.* [Wang J C, Lu M, Esteves D, Habibi M, Alna'washi G and Phaneuf R A 2007 *Phys. Rev. A* **75** 062712] with a resolution of 80 meV than their theoretical results. The contributions of the two experimental unresolved transitions are distinguished in our calculations, which show that the transitions from the ground state also make significant contributions to some resonances. Our theoretical results are also in good agreement with the measurements for the first resonance with a higher resolution of 20 meV.

Keywords: photoionization, *R*-matrix method, Ar^{5+}

PACS: 32.80.Fb **DOI:** 10.1088/1674-1056/22/12/123201

1. Introduction

Photoionization (PI) of atoms and ions is of great importance in many physical fields, such as astrophysics, plasma physics, and atmospheric physics.[1] For the aluminium isoelectronic sequence, Mendoza *et al.*[2] performed an extensive evaluation of the corresponding PI cross sections in the context of the opacity project.[3] Argon is often dipped into the fusion material as the spectral diagnostic impurity to probe the central core in the inertial confinement fusion[4] and also used as cooling gas in the diverter of Tokomak.

Recently, Wang *et al.*[5] measured absolute PI cross sections for the ground configuration $1s^22s^22p^63s^23p$ of Ar^{5+} including the ground state $^2P_{1/2}$ and the metastable state $^2P_{3/2}$ at the advanced light source (ALS). The interacting-beam technique was used in combination with the synchrotron radiation generated by an undulator with the Ar^{5+} ions produced by an electron cyclotron resonance (ECR) ion source, and the theoretical spectrum using the Cowan atomic structure code[6] was also presented for the 3s–*n*p PI processes. However, remarkable discrepancies can be found between their theoretical spectrum and experimental results. Therefore, it is necessary to perform new calculations using our recently developed relativistic *R*-matrix code, on the assumption that the ground state $^2P_{1/2}$ and the metastable state $^2P_{3/2}$ are populated as their statistical weights, since the energy difference between these two states is only 0.27 eV.[7] The present calculations are in good agreement with the experimental PI cross sections.

The rest of this paper is organized as follows. In Section 2 we briefly outline the theoretical method used in the present calculations, including our recently developed relativistic *R*-Rmatrix program, which is referred to as the *R*-matrix code in this paper. In Section 3, we present the results and discussion about the 3s–*n*p PI processes. The conclusions are given in Section 4.

2. Theoretical methods and the *R*-matrix code

The 3s–*n*p PI process of the ground configuration of Ar^{5+} could be expressed as

$$\begin{aligned} & h\upsilon + 1s^22s^22p^63s^23p \\ \rightarrow & \begin{cases} 1s^22s^22p^63s3pnp & (\text{resonance channel}), \\ 1s^22s^22p^63s3p + e & (\text{direct channel}). \end{cases} \end{aligned} \tag{1}$$

The PI cross sections are obtained by the fully relativistic *R*-matrix approach[8–10] in this work. The Dirac Hamiltonian for the $(N+1)$-electron system can be expressed in atomic units as

$$\begin{aligned} H^{N+1} = & \sum_{i=1}^{N+1} -ic\boldsymbol{\alpha}\cdot\boldsymbol{\nabla}_i + (\boldsymbol{\beta}-1)c^2 - \frac{Z}{\boldsymbol{r}_i} \\ & + \sum_{j=i+1}^{N+1} \frac{1}{|\boldsymbol{r}_j - \boldsymbol{r}_i|}, \end{aligned} \tag{2}$$

where i and j denote the individual electrons, and $\boldsymbol{\alpha}$ and $\boldsymbol{\beta}$ are the Dirac matrices. The first three one-electron terms on the right-hand side in the Hamiltonian are the momentum term, the mass term, and the electron–nucleus Coulomb attraction respectively. The final two-electron term represents the Coulomb electron–electron repulsion.

The wave function Ψ for any $(N+1)$-electron state, with

*Project supported by the National Natural Science Foundation of China (Grant Nos. 11179041 and 11275029).
†Corresponding author. E-mail: yzqu@ucas.ac.cn
© 2013 Chinese Physical Society and IOP Publishing Ltd

total energy E could be expanded as

$$\Psi = \sum_k A_{Ek}\Psi_k. \tag{3}$$

The energy-independent basis Ψ_k is given by

$$\begin{aligned}&\Psi_k(x_1\cdots x_{N+1})\\ &= \hat{A}\sum_{ij} c_{ijk}\overline{\Phi}_i(x_1\cdots x_N;\hat{r}_{N+1}\sigma_{N+1})\frac{1}{r_{N+1}}u_{ij}(r_{N+1})\\ &\quad + \sum_j d_{jk}\phi_j(x_1\cdots x_{N+1}),\end{aligned} \tag{4}$$

where $\hat{A}$ is the antisymmetrization operator to account for the exchange effects between the target electrons and the free electron; x_i represents the spatial and spin coordinates of the i-th electron; u_{ij} is the continuum orbital basis; the channel function $\bar{\Phi}_i$ is generated by coupling the target states with the angular and spin parts of the scattered electron; ϕ_j is the correlation function constructed by the bound orbitals to ensure completeness of the total wave function.

The bound orbitals are obtained from the relativistic self-consistent field (RSCF) calculation of multiconfiguration Dirac–Fock (MCDF) code GRASP2K[11] using an extended optimized level (EOL) scheme for the relevant energy levels of the target. The relativistic electron wave function has the form

$$\varphi(r) = \frac{1}{r}\begin{pmatrix} P_{n\kappa}(r)\chi^m_\kappa(\theta,\phi)\\ \mathrm{i}Q_{n\kappa}(r)\chi^m_{-\kappa}(\theta,\phi)\end{pmatrix}, \tag{5}$$

where $P_{n\kappa}(r)$ and $Q_{n\kappa}(r)$ are the large and small component radial wave functions respectively and the functions $\chi^m_{\pm\kappa}(\theta,\phi)$ are the spinor spherical harmonics. The radial wave functions (i.e. $P_{n\kappa}(r)$ and $Q_{n\kappa}(r)$) are input into the relativistic R-matrix (RRM) code in a suitable form.

The scattering calculations are performed using our newly developed R-R matrix programs, which are comprised of the internal region portions of the Dirac Atomic R-matrix Codes (DARC)[12,13] and the external region parts of the traditional Breit–Pauli (BP) R-matrix code.[14–20] In order to combine these two sets of programs, the Hamiltonian matrix elements and the dipole matrix elements obtained from the inner-region DARC code for a given $J\pi$ symmetry are reformatted to match those in the BP R-matrix code.

3. Results and discussion

In this work, the Ar^{6+} target wave functions are described by a closed core $1s^22s^22p^6$ and 19 active orbitals consisting of 5 physical orbitals $3s_{1/2}$, $3p_{1/2}$, $3p_{3/2}$, $3d_{3/2}$, $3d_{5/2}$ together with 14 pseudo-orbitals $\overline{4s}_{1/2}$, $\overline{4p}_{1/2}$, $\overline{4p}_{3/2}$, $\overline{4d}_{3/2}$, $\overline{4d}_{5/2}$, $\overline{4f}_{5/2}$, $\overline{4f}_{7/2}$, $\overline{5s}_{1/2}$, $\overline{5p}_{1/2}$, $\overline{5p}_{3/2}$, $\overline{5d}_{3/2}$, $\overline{5d}_{5/2}$, $\overline{5f}_{5/2}$, and $\overline{5f}_{7/2}$. All these orbitals are obtained by using an EOL scheme for the lowest 14 levels of Ar^{6+}. In the RSCF calculation, the configuration bases are generated by allowing double-electron excitation from the reference configurations including $3s^2$, 3s3p, $3p^2$, and 3s3d into the $n = 3,4,5$ orbitals. In the close-coupling calculation, the target wave functions are generated by allowing all the single and double excitations from the base configuration $1s^22s^22p^63s^2$ into the active orbitals $n = 3,4,5$, and the lowest 14 levels of them are included in the generation of channels. Our calculated energy levels are in good agreement with the NIST data[7] within about 1% as shown in Table 1. All the scattering calculations are performed with 6 continuum basis functions and a boundary radius of 6.56 Bohr radii. For the $^2P^o_{1/2}$ initial ground state, the dipole selection rule requires the dipole transition matrices $1/2^o \to 1/2^e$, $3/2^e$ to be included, whereas in the case of the metastable $^2P^o_{3/2}$ initial state, the dipole matrices for the transitions $3/2^o \to 1/2^e$, $3/2^e$, $5/2^e$ are required. The theoretical energies of Ar^{6+} are shifted toward experimental values in the diagonalization process of the Hamiltonian matrix in order that the energy positions of resonances relative to each ionization threshold can be improved. To resolve narrow resonances, a very fine energy mesh of 3.6 μeV is employed. The ionization potentials (IPs) for the $^2P^o_{1/2}$ and the $^2P^o_{3/2}$ terms are 91.09 eV and 90.81 eV respectively, which are in good agreement with the experimental values 91.29 eV and 91 eV by about 0.2%.

Table 1. The lowest fourteen energy levels of the target Ar^{6+}, in units of eV. Δ denotes the percentage difference between our result and the NIST value, $(E_{\mathrm{theo}} - E_{\mathrm{NIST}})/E_{\mathrm{NIST}}$.

No.	Target	NIST data	This work	Δ
1	$3s^2{}^1S^e_0$	0.0000	0.0000	
2	$3s3p^3P^o_0$	14.0227	13.9001	−0.87%
3	$3s3p^3P^o_1$	14.1225	14.0035	−0.84%
4	$3s3p^3P^o_2$	14.3313	14.2190	−0.78%
5	$3s3p^1P^o_1$	21.1668	21.4098	1.15%
6	$3p^2{}^1D^e_2$	32.8247	32.7258	−0.30%
7	$3p^2{}^3P^e_0$	33.4554	33.5185	0.19%
8	$3p^2{}^3P^e_1$	33.5721	33.6379	0.20%
9	$3p^2{}^3P^e_2$	33.7934	33.8646	0.21%
10	$3p^2{}^1S^e_0$	39.2679	39.5183	0.64%
11	$3s3d^3D^e_1$	40.1838	40.2722	0.22%
12	$3s3d^3D^e_2$	40.1884	40.2788	0.22%
13	$3s3d^3D^e_3$	40.1963	40.2887	0.23%
14	$3s3d^1D^e_2$	45.9106	46.3138	0.88%

Using the RRM code and adopting the orbital and configuration bases mentioned above, the 3s–np PI cross sections of Ar^{5+} are calculated in an energy range of 90 eV–112 eV, and compared with the experimental and theoretical results[5] in Fig. 1. The experimental and theoretical cross sections in Fig. 3 of Ref. [5] are reproduced here, which are shown in panels (a) and (b) respectively. Our PI cross sections are convoluted with a Gaussian profile of 80-meV full width at half maximum (FWHM) according to the experimental resolution. In order to compare directly with the experimental data, the energy scales have been shifted by 0.19 eV to the

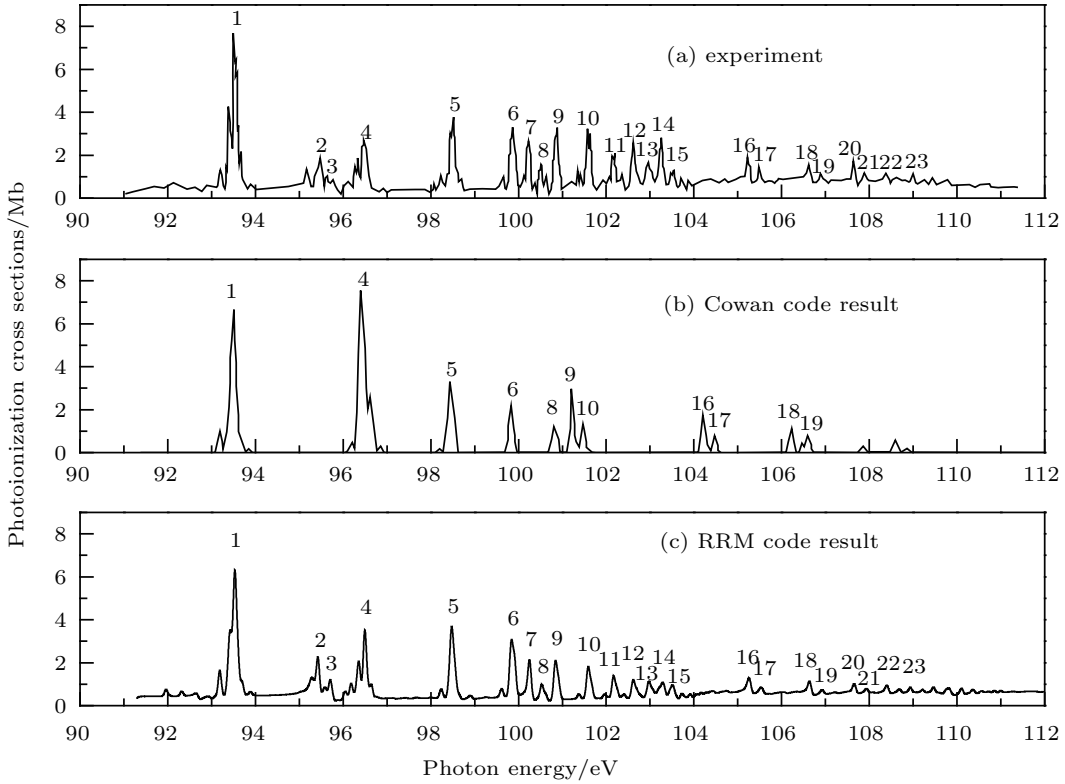


Fig. 1. Comparisons of our calculated total cross sections with their experimental and theoretical results.[5] (a) The experimental spectrum;[5] (b) the PI cross sections from the Cowan code;[5] (c) our theoretical total cross sections. The unit 1 b = 10^{-28} m^2.

high-energy side, compared with 1.23 eV in their calculations. Also, our theoretical total cross sections are obtained from the sum of the state-selective cross sections of the ground state multiplied by 1/3, and those of the metastable states multiplied by 2/3, since the energy separation between these two states is only 0.27 eV. The cross sections obtained from the length and velocity gauges are in good agreement with each other, then only the results corresponding to the length gauge are shown in the figure.

From Fig. 1, one can find that all the major resonances observed in the experimental spectrum are well reproduced in our calculations, which are shown in Figs. 1(a) and 1(c) respectively, while such resonances as 2, 3, 7, 12, 13 in the experimental results are invisible in their theoretical spectrum shown in Fig. 1(b). These can be attributed to the inaccuracy of the resonance position or the oscillator strength f. From Table 1 in Ref. [5], their theoretical oscillator strengths of resonances 1, 2, 3, and 4 are 0.0055, 0.0026, 0.0016, and 0.0035 respectively, which implies that resonances 2 and 3 are not very weak compared with resonance 4, and resonance 4 is weaker than resonance 1. However, in their theoretical spectra, resonance 4 looks stronger than 1, and resonances 2 and 3 are not indicated. One can suppose that their theoretical resonance positions for resonances 2 and 3 are quite close to resonance 4, and then the strong resonance 4 in Fig. 1(b) actually arises from contributions of resonances 2–4. In fact, the sum of their theoretical oscillator strengths of resonances 2, 3, and 4 is 0.0077 which is larger than the f value 0.0055 of resonance 1. Our integrated intensities of resonances 1 and 4 have a ratio of 163:91, which is close to the experimental results of 82:39. Similarly, from Table 1 in Ref. [5], their theoretical oscillator strengths of resonances 6, 7, 8, and 9 are 0.0017, 0.0015, 0.0009, and 0.0011 respectively, which implies that resonance 7 is not very weak compared with resonance 6, while resonance 9 is weaker than resonance 6. However, in their theoretical spectra, resonance 9 looks stronger than resonance 6, and resonance 7 is invisible, although the reason is not clear. Also, our calculated energy positions for resonances 8, 9, 10, 16–19 are in better agreement with the experimental results. On the other hand, the discrepancy between their experimental and theoretical results may also be due to inaccurate calculations for the f values. From Table 1 in Ref. [5], their calculated oscillator strengths for resonances 12 and 13 are both equal to 0.0003, which are much weaker than the experimental results 0.0012 and 0.0008 respectively, thus these two resonances are invisible in their theoretical spectra.

In Fig. 2 the state-selective cross sections for the ground state $^2P^o_{1/2}$ and the metastable state $^2P^o_{3/2}$ with photon energies ranging from 90 eV to 112 eV are displayed, and compared with the measured total cross sections. For comparison, the energy scale has been shifted by 0.19 eV to the higher-energy side, and the theoretical cross sections are convoluted with a Gaussian profile of 80-meV FWHM. The measured resonances have been identified as three Rydberg series in Ref. [5]. Resonances 1, 4, 5, 6, 9–15 belong to the first Rydberg series of the two unresolved transitions $3s^23p(^2P_{3/2}) - 3s3p(^3P)np(^2D_{5/2})$

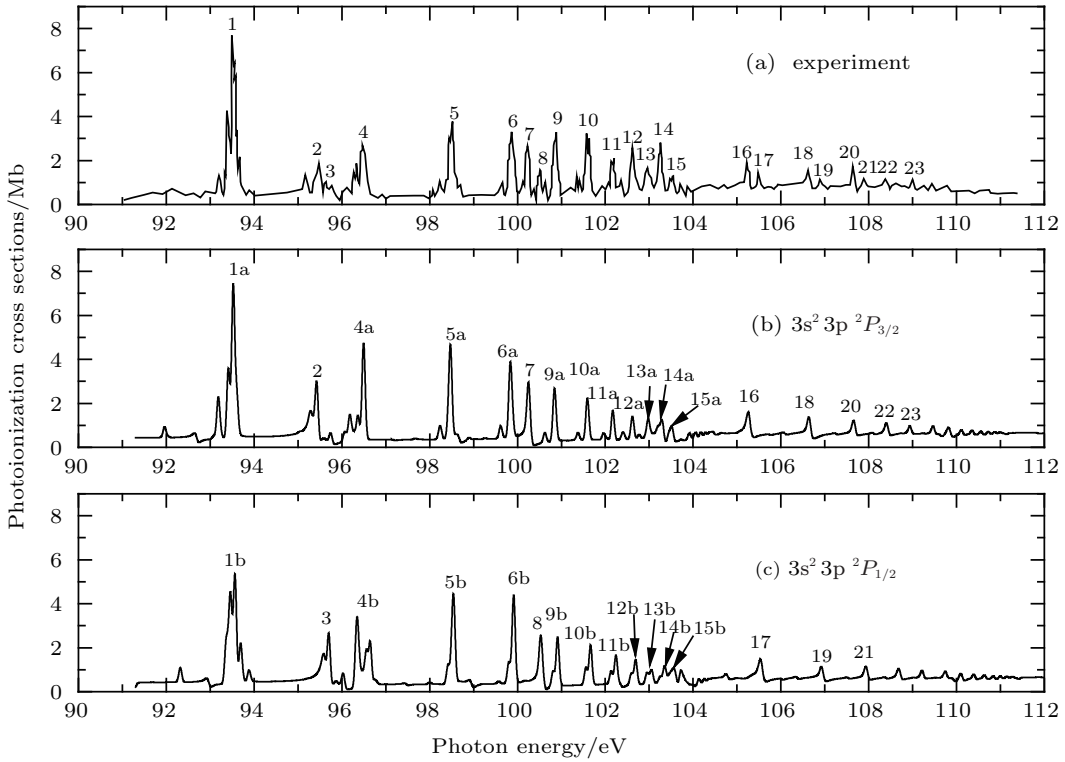


Fig. 2. Comparisons between our state-selective cross sections and the measurements[5] with a resolution of 80 meV. (a) The experimental spectrum;[5] (b) our state-selective cross sections for the metastable state $^2P^o_{3/2}$; (c) our state-selective cross sections for the ground state $^2P^o_{1/2}$.

$(n > 6)$ (transition 1) and $3s^23p(^2P_{1/2}) - 3s3p(^3P)np(^2D_{3/2})$ $(n > 6)$ (transition 2). Resonances 2, 7, 14, 16, 18, 20, 22, and 23 belong to the second Rydberg series of the transitions $3s^23p(^2P_{3/2}) - 3s3p(^1P)np(^2D_{5/2})$ $(n > 5)$, and resonances 3, 8, 15, 17, 19, and 21 belong to the third Rydberg series of the transitions $3s^23p(^2P_{1/2}) - 3s3p(^1P)np(^2D_{3/2})$ $(n > 5)$. The first Rydberg series is much stronger than the other two, since it is a superposition of the two unresolved transitions 1 and 2. Taking the first three transitions of the first Rydberg series (i.e. $3s^23p(^2P_{3/2}$ or $^2P_{1/2}) - 3s3p(^3P)np(^2D_{5/2}$ or $^2D_{3/2})$ $(n = 7, 8, 9)$) for example, we elaborate the reason why transitions 1 and 2 are unresolved. The fine structure energy splitting of the initial states $3s^23p(^2P_{3/2})$ and $3s^23p(^2P_{1/2})$ is 0.27 eV,[20] and that of the final states $3s3p(^3P)np(^2D_{5/2})$ and $3s3p(^3P)np(^2D_{3/2})$ $(n = 7, 8, 9)$ is about 0.23 eV according to our calculations using GRASP2K,[11] which are shown in Table 2. Thus the transition energy difference between transitions 1 and 2 is about 0.04 eV, which is less than the experimental resolution of 0.08 eV. But these two transitions can be distinguished in our calculations, then the contributions of transitions 1 and 2 are shown in Figs. 2(b) and 2(c). In Ref. [5], resonances 12, 13, and 14 are attributed to the transitions from only the initial metastable state $^2P^o_{3/2}$, while in our calculations, the ratios of the integrated intensities of resonances 12b, 13b, 14b from $^2P^o_{1/2}$ to those of resonances 12a, 13a, 14a from $^2P^o_{3/2}$ are about 48:43, 15:14, and 5:6, respectively. Therefore, the transitions from the ground state $^2P^o_{1/2}$ also make significant contributions to these resonances, and should not be ignored.

Table 2. Eigenenergies of $3s3p(^3P)np(^2D_{5/2})$ and $3s3p(^3P)np(^2D_{3/2})$ $(n = 7–9)$ in unit eV, Δ denotes the energy difference between $3s3p(^3P)np(^2D_{5/2})$ and $3s3p(^3P)np(^2D_{3/2})$, $E_{^2D_{5/2}} - E_{^2D_{3/2}}$.

	$3s3p(^3P)np(^2D_{5/2})$	$3s3p(^3P)np(^2D_{3/2})$	Δ
$n = 7$	−14082.16	−14082.40	0.24
$n = 8$	−14079.20	−14079.43	0.23
$n = 9$	−14077.23	−14077.46	0.23

In Ref. [5], the experimental spectrum of the resonance 1 with a higher resolution of 20 meV is also presented, along with theoretical results using Cowan's code, which are compared with our results as shown in Fig. 3. Both theoretical PI cross sections are convoluted with a Gaussian profile of 20-meV FWHM and statistically weighted. In Table 3 the theoretical resonance positions and oscillator strengths are compared with the experimental results for the resonances in Fig. 3. Our theoretical resonance positions are determined from the peaks of resonances, and the oscillator strengths are obtained by integration.

Our theoretical results are in much better agreement with the experiment results. For instance, resonances a, b, d and e are reproduced well in our calculations, while in their theoretical results in Fig. 3(a) resonances a and b merge into one, and one more resonance appears between resonances d and e, which cannot be found in the experimental results. For resonance c, our theoretical oscillator strength 0.0005 is close to the experimental value 0.0007, compared with their theoretical value 0.0002. Furthermore, our results provide better energy position and f value for resonance g.

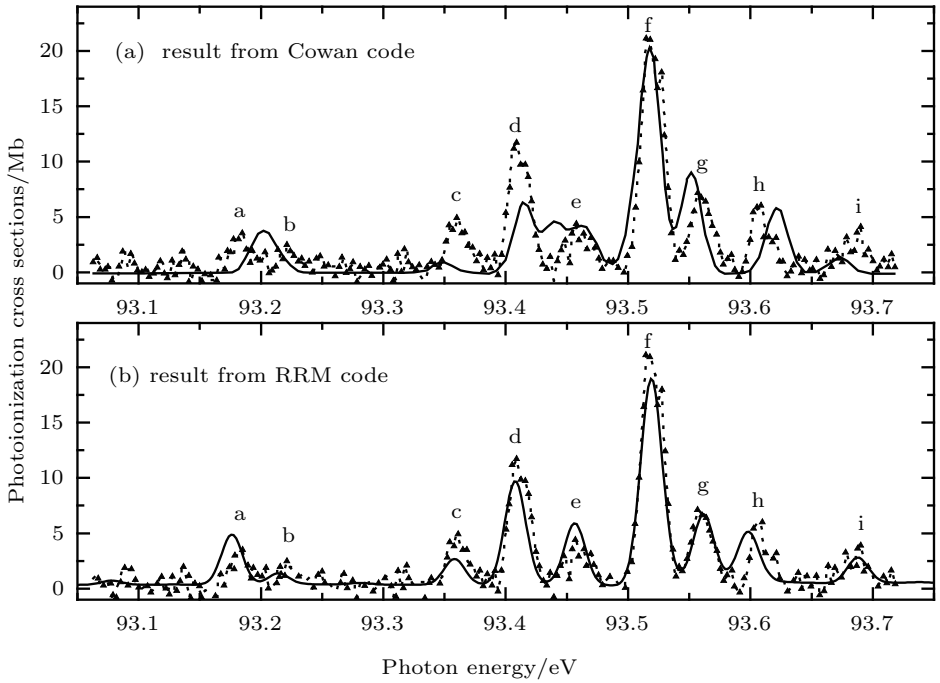


Fig. 3. Comparison between theoretical results and experimental measurements[5] for the first resonance in Fig. 1. In both panels, the dotted curves with triangle symbols denote the experimental results,[5] taken at a resolution of 20 meV; the solid curves represent the theoretical PI cross sections. (a) The PI cross sections from the Cowan code;[5] (b) our theoretical PI cross sections.

Table 3. Comparisons of theoretical resonance positions and oscillator strengths with the experimental results for the resonances in Fig. 3.

Feature	Position/eV (Expt.)[5]	Position/eV (this work)	f value (Expt.)[5]	Theoretical f value[5]	f value (this work)
a	93.18	93.18	0.0005	0.0005	0.008
b	93.22	93.21	0.0003	0.0001	0.0003
c	93.36	93.36	0.0007	0.0002	0.0005
d	93.41	93.41	0.0019	0.0012	0.0018
e	93.46	93.46	0.0007	0.0005	0.0010
f	93.52	93.52	0.0041	0.0038	0.0035
g	93.56	93.56	0.0014	0.0017	0.0012
h	93.61	93.60	0.0010	0.0011	0.0010
i	93.69	93.69	0.0004	0.0003	0.0005

4. Conclusions

In this paper, we investigate the 3s–np PI processes of the ground configuration of Ar^{5+}, using our recently developed relativistic R-matrix code, where the interactions between the bound states and the continuum states are included. Our results are in better agreement with the recent measurements,[5] and show a great improvement on their theoretical results using the Cowan code considering only interactions among the bound states. For resonances like 2, 3, and 7 better resonance positions are provided, and for resonances like 12 and 13 better f values are obtained. The two experimental unresolved transitions 1 and 2 are distinguished in our calculations, which show that the transitions from the ground state $^2P^o_{1/2}$ also make significant contributions to resonances 12, 13, and 14. For resonance 1, our theoretical results are also in much better agreement with the measurements at a higher resolution of 20 meV.[5]

References

[1] Wang G L and Zhou X X 2009 *Chin. Phys. B* **18** 3833
[2] Mendoza C, Eissner W, Dourneuf M L and Zeippen C J 1995 *J. Phys. B* **28** 3485
[3] Seaton M J 1987 *J. Phys. B* **20** 6363
[4] Amendt P, Landen O L, Robey H F, Li C K and Petrasso R D 2010 *Phys. Rev. Lett.* **105** 115005
[5] Wang J C, Lu M, Esteves D, Habibi M, Alna'washi G and Phaneuf R A 2007 *Phys. Rev. A* **75** 062712
[6] Cowan R D 1981 *The Theory of Atomic Structure and Spectra* (Berkeley: University of California Press)
[7] Ralchenko Y, Kramida A E, Reader J and NIST ASD Team 2010 NIST Atomic Spectra Database (version 4.0.1), National Institute of Standards and Technology, Gaithersburg, MD [http://physics.nist.gov/asd]
[8] Chang J J 1975 *J. Phys. B* **8** 2327
[9] Chang J J 1977 *J. Phys. B* **10** 3195
[10] Norrington P H and Grant I P 1981 *J. Phys. B* **14** L261
[11] Jonsson P, He X, Fischer C F and Grant I P 2007 *Comput. Phys. Commun.* **177** 597
[12] Norrington P H and Grant I P 1987 *J. Phys. B* **20** 4869
[13] Ait-Tahar S, Grant I P and Norrington N H 1996 *Phys. Rev A* **54** 3984
[14] Burke P G, Hibbert A and Robb W D 1971 *J. Phys. B* **4** 153
[15] Berrington K A, Burke P G, Chang J J, Chivers A T, Robb W D and Taylor K T 1974 *Comput. Phys. Commun.* **8** 149
[16] Berrington K A, Burke P G, Dourneuf M, Robb W D, Taylor K T and Voky L 1978 *Comput. Phys. Commun.* **14** 367
[17] Berrington K A, Burke P G, Butler K, Seaton M J, Storey P J, Taylor K T and Yan Y 1987 *J. Phys. B* **20** 6379
[18] Voky L, Saraph H E, Eissner W, Liu Z W and Kelly H P 1992 *Phys. Rev. A* **46** 3945
[19] Berrington K A and Kingston A E 1987 *J. Phys. B* **20** 6631
[20] Berrington K A, Eissner W B and Norrington P H 1995 *Comput. Phys. Commun.* **92** 290